# Kinetics and mechanism of antigorite dehydration: Implications for subduction zone seismicity

Mélanie Chollet, Isabelle Daniel, Kenneth T. Koga, Guillaume Morard, Bertrand van de Moortèle

# Kinetics and mechanism of antigorite dehydration: Implications for subduction zone seismicity

Mélanie Chollet,[1] Isabelle Daniel,[1] Kenneth T. Koga,[2] Guillaume Morard,[3,4] and Bertrand van de Moortèle[1]

Received 29 May 2010; revised 4 January 2011; accepted 13 January 2011; published 8 April 2011.

[1] Properties of serpentine minerals are thought to influence the occurrence and location of intermediate-depth seismicity in subduction zones, which is often characterized by two dipping planes separated by ~30 km defining a double seismic zone. The seismicity of the lower plane is believed to be provoked by the dehydration of serpentine since the experimentally determined stability limit for antigorite matches hypocenter locations. This requires that the fluid produced by dehydration is released much faster than the typical time scale of ductile deformation mechanisms. Here we measured the kinetics of antigorite dehydration in situ at high pressure and high temperature by time-resolved synchrotron X-ray diffraction in a closed system. Antigorite dehydrates in two steps. During step 1 it partially breaks down into olivine and a hydrous phyllosilicate closely related to the 10 Å phase. The modal abundance of the intermediate assemblage is described by 66 wt % antigorite, 19 wt % olivine, 12 wt % 10 Å phase. During step 2 at higher temperature, the remaining antigorite and the 10 Å phase fully dehydrate. From the analysis of reaction progress data, we determined that the major release of aqueous fluid occurs during step 2 at a fast rate of $10^{-4}$ $m^3_{fluid}$ $m^{-3}_{rock}$ $s^{-1}$. This exceeds by orders of magnitude the typical time scale of deformation by ductile mechanisms of any mineral or rock in the subducting slab or in the overlying mantle wedge. These results suggest that the fast dehydration of antigorite may well trigger the seismicity of the lower plane of the double seismic zone.

**Citation:** Chollet, M., I. Daniel, K. T. Koga, G. Morard, and B. van de Moortèle (2011), Kinetics and mechanism of antigorite dehydration: Implications for subduction zone seismicity, *J. Geophys. Res.*, *116*, B04203, doi:10.1029/2010JB007739.

## 1. Introduction

[2] In most subduction zones, intermediate-depth seismicity (50–200 km depth) organizes along two dipping planes within the subducting slab, defining a double seismic zone (DSZ) [*Brudzinski et al.*, 2007; *Dorbath et al.*, 2008; *Hasegawa et al.*, 1978]. The separation between the upper and lower planes increases with plate age from 8 to 30 km, for 12 Ma old and 160 Ma old slabs, respectively [*Brudzinski et al.*, 2007]. This seismicity is thermally activated and most likely caused by dehydration embrittlement [*Dobson et al.*, 2002; *Hacker et al.*, 2003; *Omori et al.*, 2002; *Peacock*, 2001; *Yamasaksi and Seno*, 2003]. The upper plane of the DSZ is part of the Wadati-Benioff zone and is related to the dehydration of metabasalts during eclogite formation. The seismicity of the lower plane located in the subducting serpentinized mantle is most frequently interpreted as the result of the dehydration of antigorite [*Hacker et al.*, 2003; *Peacock*, 2001].

[3] Antigorite is the high-pressure variety of serpentine, stable at intermediate depth in the subducting slab [*Bose and Navrostsky*, 1998; *Bromiley and Pawley*, 2003; *Hilairet et al.*, 2006; *Peacock*, 2001; *Ulmer and Trommsdorff*, 1995; *Wunder and Schreyer*, 1997]. Antigorite commonly occurs in association with highly metamorphosed mafic and ultramafic rocks in paleosubduction zones such as the Alps, Cuba and the Betic Cordillera, SE Spain [*Guillot et al.*, 2001; *Hermann et al.*, 2000]. Serpentine mostly form during hydrothermal alteration of ultramafic rocks, and contains 13 wt % $H_2O$, one of the highest water content among hydrous silicates. Consequently, they play a key role in water transport into the deep mantle [e.g., *Rüpke et al.*, 2004].

[4] Dehydration of antigorite has been proposed to explain the DSZ lower plane because lower plane earthquake hypocenters are roughly aligned along the estimated locations of 600–650°C isotherms [*Peacock*, 2001; *Yamasaksi and Seno*, 2003], which corresponds to the experimentally determined limit of antigorite stability [*Ulmer and Trommsdorff*, 1995].

[1]Laboratoire de Géologie de Lyon: Terre, Planètes, Environnement, Université Lyon 1, Ecole Normale Supérieure de Lyon, CNRS, UMR 5276, Villeurbanne, France.
[2]Laboratoire Magmas et Volcans, UMR CNRS 6524, IRD M163, Université Blaise Pascal Clermont-Ferrand, Clermont-Ferrand, France.
[3]European Synchrotron Radiation Facility, Grenoble, France.
[4]Institut de Minéralogie et de Physique des Milieux Condensés, Paris, France.


0148-0227/11/2010JB007739

Although such a dehydration reaction definitely has seismogenic potential, this mechanism requires release of aqueous fluid by the dehydration reaction at a rate faster than the time scale of viscous relaxation of solid matrix. In this study we have measured the kinetics of dehydration of antigorite in a closed system using in situ time-resolved experiments. This provides additional constraints on the fluid production rate due to serpentine dehydration and on the root cause of intermediate depth seismicity in subduction zones.

## 2. Methods

### 2.1. In Situ Time-Resolved Dehydration Experiments

[5] The sample consisted of a natural antigorite $Mg_{2.62}Fe_{0.16}Al_{0.19}Si_{1.96}O_5(OH)_4$ containing 3.45 wt % $Al_2O_3$ and 4.15 wt % FeO [*Auzende et al.*, 2004], with ~0.1 wt % pure water added in excess. It was loaded in a Ti capsule cold-sealed with Au lids closing the system with respect to water and major oxides [*Chinnery et al.*, 1999; *Chollet et al.*, 2009]. *Chollet et al.* [2009] previously showed that the dehydration of talc was reversible in this assembly, demonstrating the presence of free water in a similar Ti-Au capsule. The whole cell assembly, identical to that described by *Chollet et al.* [2009], was placed between the tungsten carbide anvils of a Paris-Edinburgh press. This press is an opposed anvils device that was first developed for neutron diffraction [*Besson et al.*, 1992] and subsequently adapted for X-ray diffraction [*Mezouar et al.*, 1999]. Time-resolved angle dispersive X-ray diffraction experiments were performed at the high-pressure beam line ID27 of the European Radiation Synchrotron Facility (ESRF, Grenoble, France). High-quality 30 s XRD patterns were acquired, every 3 to 4 min during reaction. The patterns were analyzed with the GSAS package [*Larson and Von Dreele*, 2004]; phases were identified and their unit cell parameters were refined by the Le Bail method [*Le Bail et al.*, 1988].

[6] Mixed powders of Au and NaCl placed in a 0.5 mm side hole drilled in the h-BN sleeve of the capsule were used as pressure ($P$) and temperature ($T$) gauges. Their XRD pattern was measured periodically during the experiments, but priority was given to reaction progress measurements. Pressure and temperature conditions were calculated from the cross calibration method using the thermal equations of state of *Takemura* [2001] and *Yamamoto et al.* [1987] for Au and NaCl, respectively [*Crichton and Mezouar*, 2002]. Reported ($P$, $T$) conditions correspond to either individual measurements or averages of two bracketing ($P$, $T$) condition measurements. Uncertainties in $P$ and $T$ depend on both the errors in the unit cell volume of Au and NaCl of typically $7 \times 10^{-3}$ Å$^3$, and the errors in the thermoelastic parameters of calibrants. Resulting errors are much larger than those induced by temperature gradients in the sample [*Morard*, 2006]. We obtain a combined precision and accuracy of pressure and temperature measurements of ±0.2 GPa, and ±73°C ($2\sigma$), respectively. Consequently, uncertainties on ($P$, $T$) conditions in the present in situ study are much larger than in ex situ experiments at similar conditions (typically 0.1 GPa and 10°C) that take advantage of measuring temperature with a thermocouple.

[7] The sample was first compressed at room temperature to the target pressure of ~4 GPa corresponding to oil pressure of 350 bar on the anvils, which was kept constant throughout the experiment. Then, temperature was slowly increased at 3°C min$^{-1}$ until the first peaks of reactants appear in the XRD pattern. Run conditions, i.e., oil pressure and power delivered to the furnace were then maintained constant at 350 bars and 167 W, respectively, until the first step of antigorite dehydration was completed (see below). The corresponding sample pressure and temperature were measured afterward. Meanwhile, isothermal XRD spectra were periodically acquired. Then, temperature was again slowly increased at ~1°C min$^{-1}$, until the second step of the reaction began, i.e., when peaks of the intermediate phases decreased in intensity and peaks of the final products appeared on XRD patterns. Run conditions, i.e., oil pressure and power delivered to the furnace were maintained constant at 350 bars and 204 W, respectively, until completion of dehydration as determined from the disappearance of antigorite peaks in XRD patterns. A second series of isothermal XRD patterns were acquired to constrain the kinetics of this reaction.

### 2.2. Ex Situ Observation of Quenched Samples

[8] An additional experiment was carried out offline in a belt press to synthesize the intermediate assemblage. Similar antigorite powder and ~0.1 wt % water were loaded in a Au-Ta double capsule that seals upon compression [*Koga et al.*, 2005]. The sample was annealed at 4.5 ± 0.5 GPa, 580 ± 25°C (conditions estimated from calibration curves), within the intermediate stage of antigorite dehydration, as determined from the in situ experiment. It was quenched after 80 min reaction.

[9] Quenched samples were observed by backscattered electron (BSE) microscopy, with a JEOL 840 scanning electron microscope (SEM) at the MATEIS laboratory (Lyon, France). They were also analyzed by Raman spectroscopy in the backscattered geometry with a Jobin Yvon® LabRam HR800 visible spectrometer at an incident wavelength of 514.32 nm delivered by an $Ar^+$ laser (Spectra Physics®). An optical microscope was used to focus the incident beam into a 2$\mu$m diameter spot on the sample. Spectra were acquired in 3 acquisitions of 100 s in two spectral windows, 175–1175 cm$^{-1}$ and 3400–3800 cm$^{-1}$, permitting characterization of the lattice and internal modes as well as the symmetric stretching vibrations of hydroxyls.

## 3. Results and Discussion

### 3.1. Phase Relations During Antigorite Breakdown

[10] We observe that the dehydration of antigorite occurs as a two-step reaction. The first XRD pattern (indicated as 0 min, Figure 1) was acquired just before the reaction started and serves as a reference. The XRD pattern displays the diffraction peaks of antigorite and some minor contributions from the cell assembly. The second pattern in Figure 1 (110 min) depicts the assemblage characteristic of the intermediate stage after completion of the first step of the reaction. During this first step, antigorite transforms partially into olivine and a second phase characterized by a large d spacing of 9.57 Å distinctive of the basal distance of a hydrous phyllosilicate. The third spectrum in Figure 1

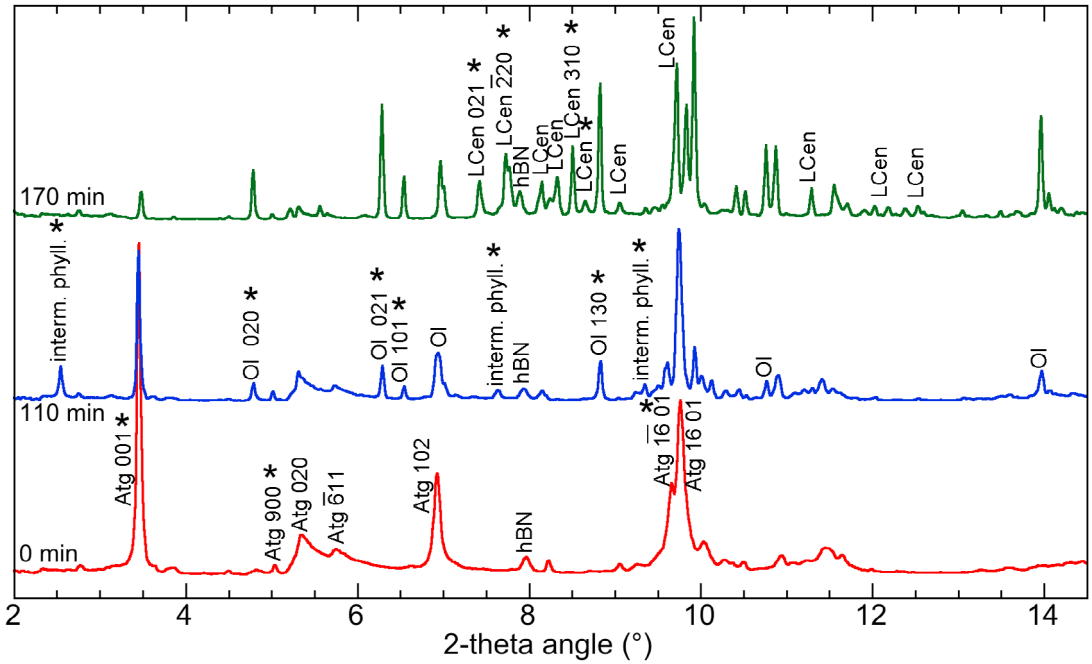


**Figure 1.** X-ray diffraction patterns of antigorite dehydration at three different stages: before the reaction started, during the intermediate stage at 110 min, and during step 2 at 170 min. Peaks are labeled according to minerals: Atg, antigorite; interm. phyll., the intermediate 10 Å phase; Ol, olivine; hBN, hexagonal boron nitgride; and LCen, low clinoenstatite. Stars refer to the selected peaks used to calculate the representative cumulative intensity of each phase involved in the reactions.

(170 min) reflects the assemblage after temperature was subsequently slowly increased, and the second step of the reaction started. During this second step of the reaction, XRD peaks of antigorite and of the intermediate phase progressively decrease in intensity, while those of olivine and low clinoenstatite grow. Consequently, the in situ investigation of antigorite dehydration under water saturation indicates that it proceeds in two steps:

Step 1

$$\text{Antigorite} \rightarrow \text{intermediate phase} + \text{olivine} + \text{fluid}$$

Step 2

$$\text{Antigorite} + \text{intermediate phase} \rightarrow \text{olivine} + \text{low clinoenstatite} + \text{fluid}$$

The summed intensities of selected diffraction peaks of the four phases observed during antigorite dehydration are presented as a function of time and temperature in Figure 2. Step 1 occurs at 4.5 GPa, 567°C and stops after ~35 min. Pressure and temperature conditions of step 1 were inferred from XRD patterns measured on the Au-NaCl ($P$, $T$) gauges after completion of step 1 at a constant power of 167 W. During the intermediate stage, the summed intensities of the selected XRD peaks of both olivine and the intermediate phase remain constant. The summed intensities of the selected XRD peaks of antigorite still slightly decrease, likely due to reorientation of antigorite crystals. The intensity of antigorite ($hk0$) lines remains constant whereas basal ($00l$) strong intensities diminish. This indicates a reduction of the preferred orientation during the intermediate stage, whereas preferred orientation usually develops upon compression of a phyllosilicate with the sheets orthogonal to the maximum stress axis [*Niskanen*, 1964]. This stress-free recrystallization of antigorite suggests near-hydrostatic conditions, most likely due to the availability of free water in the capsule. Dehydration step 2 occurs at 4.1 GPa, 681°C at a constant power of 204 W, after a slow increase in temperature of 102°C at a rate of 1°C $min^{-1}$. ($P$, $T$) conditions during step 2 were obtained by interpolation between conditions before and after the start of step 2. During step 2, antigorite and the intermediate phyllosilicate phase reflections completely disappear from the XRD patterns in 40 min, in favor of olivine and low-clinoenstatite. Small amount of chlorite is also detected by Raman spectroscopy in run products. The characteristic time of step 2 is in very good agreement with that obtained by *Inoue et al.* [2009] under similar conditions.

[11] Serpentine dehydration has previously been reported as a two-step reaction on the basis of in situ experiments, with the occurrence of a phase close to talc $Mg_3Si_4O_{10}(OH)_2$ during the intermediate stage. *Perrillat et al.* [2005] and *Inoue et al.* [2009] observed a "talc-like" phase during antigorite dehydration; *Franck et al.* [2005] reported talc-like material during the breakdown of lizardite, and *Candela et al.* [2007] obtained talc as an intermediate phase during the breakdown of chrysotile. In an open system, *Perrillat et al.* [2005] observed the complete transformation of antigorite into olivine and an intermediate talc-like phase during the first step of the reaction at ~550°C, followed by the dehydration of the talc-like phase at ~670°C. In the present closed system, antigorite and the intermediate

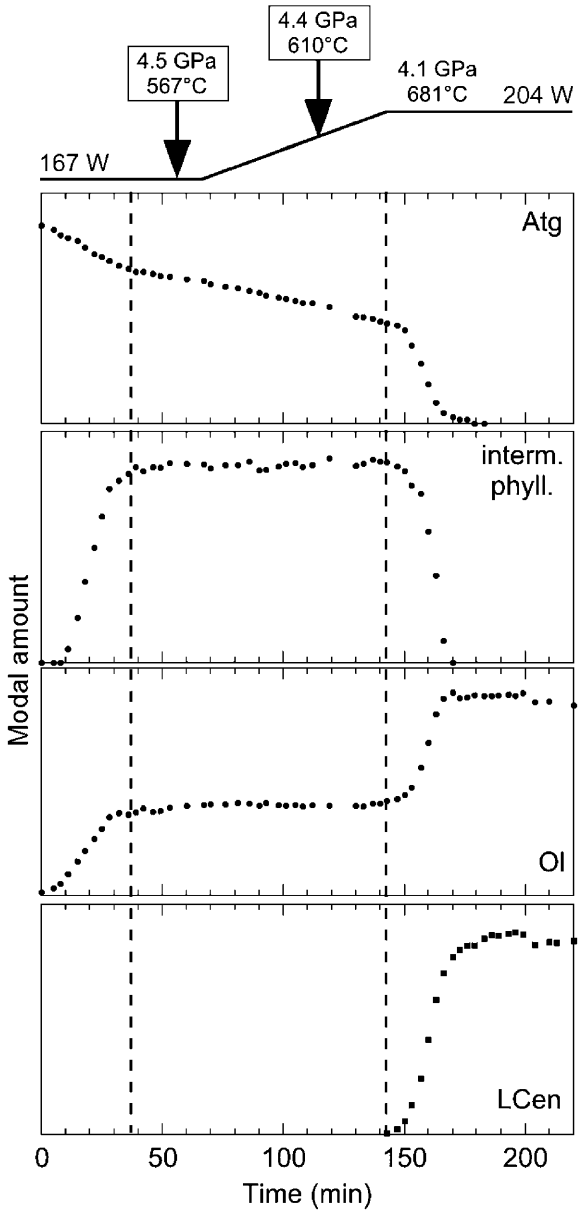


**Figure 2.** Summed intensity of selected XRD peaks of minerals involved during antigorite dehydration as a function of time. Atg, antigorite; interm. phyll., the 10 Å phase of this study; and LCen, the low clinoenstatite. The left and right vertical dashed lines show the end of step 1 and the onset of step 2, respectively. Evolution of experimental conditions are also reported, including power as a function of time, and (*P*, *T*) conditions obtained either from cross calibration (in boxes) or from interpolation between measured neighboring conditions.

hydrous phyllosilicate phase coexist during the intermediate stage. Such an intermediate stage has systematically been observed in situ, but hasn't generally been reported in quench studies [*Bromiley and Pawley*, 2003; *Eggler and Ehmann*, 2010; *Ulmer and Trommsdorff*, 1995; *Wunder and Schreyer*, 1997]. However, the presence of 10 Å phase $Mg_3Si_4O_{10}(OH)_2{\cdot}xH_2O$ ($x$ = 0.66, 1, or 2) which is closely related to talc has been reported at least twice among the dehydration products of antigorite. Using natural antigorite as the sole starting material, *Khodyrev and Agoshkov* [1986] observed dehydration of the initial serpentine to the assemblage forsterite + 10 Å phase in the 3–4 GPa range. The 10 Å phase was also described among dehydration products in some runs by *Ulmer and Trommsdorff* [1995]. Assessing the exact origin of the supposed discrepancy on the occurrence of an intermediate phyllosilicate phase during antigorite dehydration in all the abovementioned studies is beyond the scope of the present contribution. Differences in the initial amount of water in the system, in the presence/lack of reaction products in the system, in the pressure/temperature conditions and the heating rate, and in the analytical methods clearly lead to slightly different conclusions. Resolution of these differences requires extensive additional experimentation.

[12] The location of steps 1 and 2 of the dehydration reaction in (*P*, *T*) space are reported together with previously obtained stability limits of antigorite in Figure 3 [*Bose and*

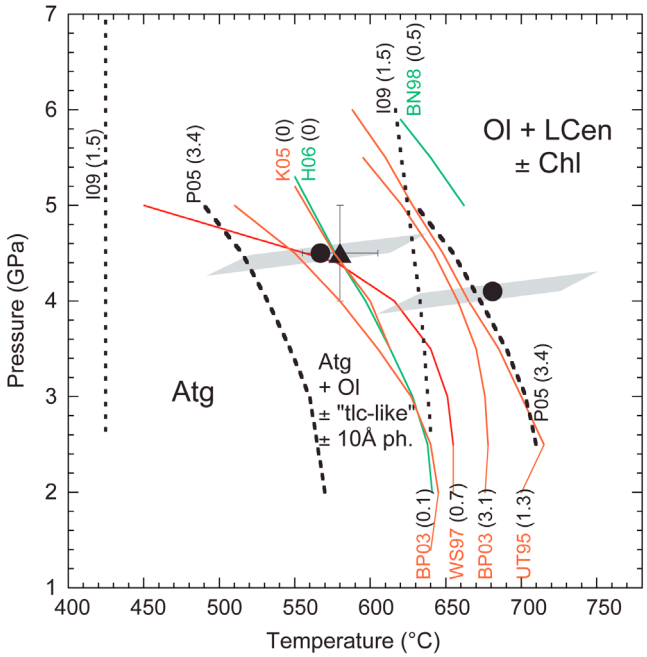


**Figure 3.** *P*, *T* conditions for antigorite dehydration. Solid red lines locate the stability limit of antigorite measured in quench studies by WS97 [*Wunder and Schreyer*, 1997], BP03 [*Bromiley and Pawley*, 2003], UT95 [*Ulmer and Trommsdorff*, 1995], and K05 [*Komabayashi et al.*, 2005]. Solid green lines locate the stability limit of antigorite calculated by H06 [*Hilairet et al.*, 2006] and BN98 [*Bose and Navrostsky*, 1998]. The fields of the "talc-like" phase, observed by P05 [*Perrillat et al.*, 2005] and I09 [*Inoue et al.*, 2009], are reported by dashed lines. The $Al_2O_3$ content of antigorite is given in parentheses. Solid circles show the onset of steps 1 and 2 of the reaction observed during the present in situ experiment. The parallelograms of uncertainties on (*P*, *T*) conditions are also reported The triangle locates (*P*, *T*) conditions of the off-line experiment. Atg, for antigorite; tlc-like, the talc-like phase; 10Å ph., 10 Å phase; Ol, olivine; LCen, low clinoenstatite; and Chl, chlorite.

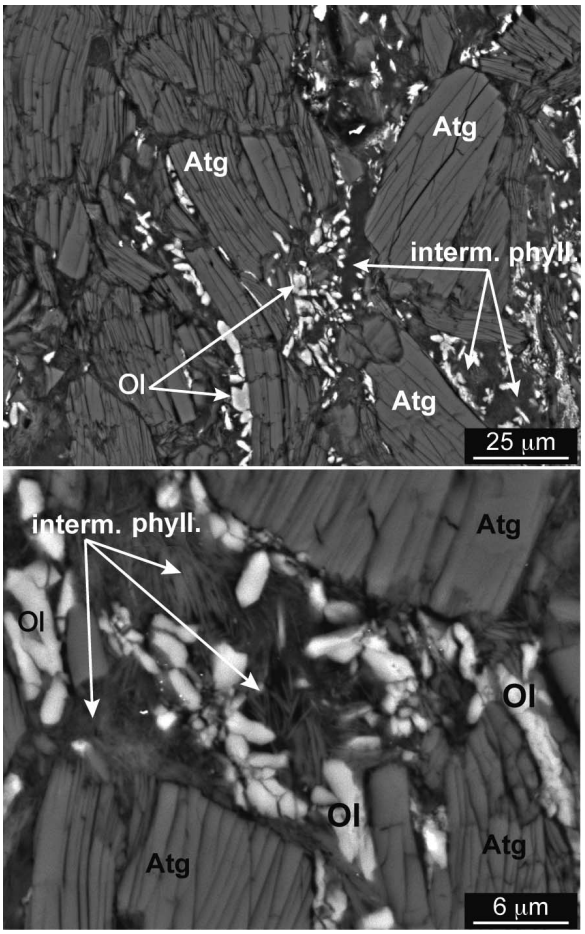


**Figure 4.** Backscattered electron images of the run product of the ex situ experiment quenched after 80 min at the intermediate stage of antigorite dehydration. Mineral abbreviations are as described in Figure 1 caption.

*Navrostsky*, 1998; *Bromiley and Pawley*, 2003; *Hilairet et al.*, 2006; *Inoue et al.*, 2009; *Perrillat et al.*, 2005; *Ulmer and Trommsdorff*, 1995; *Wunder and Schreyer*, 1997]. Although the (*P*, *T*) conditions obtained for antigorite dehydration in the present study are not precise enough to be compared one to one to the abovementioned phase diagrams derived from quench studies, Figure 3 shows a general agreement between the dehydration curves of antigorite of similar composition. The water saturation conditions affect only moderately the onset and the completion of the reactions involved in antigorite dehydration [*Perrillat et al.*, 2005].

### 3.2. Intermediate Stage and Intermediate Phase

[13] The texture of the assemblage at the intermediate stage was characterized by BSE microscopy using the run product of our ex situ experiment (Figure 4). The intermediate phase occurs as fibers of ~0.3 $\mu$m thick and 3 $\mu$m long, in which clusters of euhedral olivines ~5 $\mu$m in size are embedded. Similar fibrous to needle-like crystals were also recently described in addition to antigorite prior to dehydration at 630°C, 2 GPa [*Eggler and Ehmann*, 2010]. The Raman spectrum of the quenched intermediate phase is characterized by four bands at 3589, 3622, 3676, and 3701 $cm^{-1}$ corresponding to the symmetric stretching vibrations of hydroxyls (Figure 5). The signal of internal and lattice Raman modes below 1000 $cm^{-1}$ is too weak to be measured. Raman frequencies and basal *d*-spacing of the intermediate phase are compared in Table 1 to those of talc, of 10 Å phase, of the talc-like phase formed in the experiments of *Perrillat et al.* [2005], and of a recrystallized hydrous phyllosilicate [*Chollet et al.*, 2009]. The latter phase was synthesized during in situ rehydration of the dehydration products of talc, coesite and enstatite. In the present study, the Raman spectrum of the intermediate phase displays Raman OH stretching modes characteristic of the expanded 10 Å phase after treatment by acetone as described by *Fumagalli et al.* [2001]. Talc may also contribute to the broad intense band at 3676 $cm^{-1}$, which is larger in the present intermediate phase than in the expanded 10 Å phase. An additional peak at 3701 $cm^{-1}$ indicates the presence of isolated hydroxyls in the structure of the intermediate phase. The basal *d*-spacing for the intermediate phase at 9.57 Å (Figure 1) confirms that it is closely related to the 10 Å phase. We interpret the intermediate phase as a poorly crystallized 10 Å phase.

[14] The water content of the intermediate hydrous phase could not be measured because of the very small size of the fibrous crystals. The water content reported in the literature for the 10 Å phase varies from 7.6 to 13.1 wt % depending on the number of water molecules ($x$) in the structure, $x$ = 0.66, 1 or 2 [e.g., *Fumagalli and Stixrude*, 2007; *Wang et al.*, 2004]. The swelling behavior of the 10 Å phase in the present study is consistent with a high water content [*Fumagalli et al.*, 2001]. For synthesis duration of 1 to 2 h, *Bauer and Sclar* [1981] also reported a water content of 1 $H_2O$ per formula unit (pfu). Consequently, we assume that the intermediate phase formed in this study in the intermediate stage of the in situ experiment and in the ex situ quenched sample after 80 min contains a minimum of 1 $H_2O$ pfu, i.e., 9.1 wt %.

[15] Relative abundance of each phase in the sample after step 1 of the reaction is estimated independently from the BSE images of the quench experiment, and from the X-ray intensities during in situ experiments. In BSE images, anti-

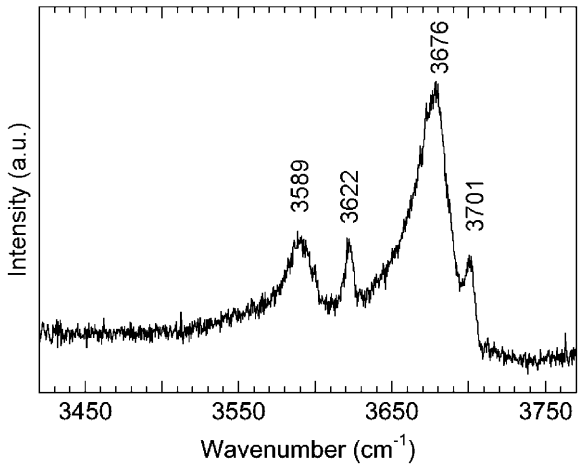


**Figure 5.** Raman spectra of the hydroxyl stretching modes of the hydrous phyllosilicate occurring during the intermediate stage of antigorite dehydration.

**Table 1.** Basal Distance and Raman Frequencies of Symmetric Stretching Vibrations of Hydroxyls in the Intermediate Phase, Compared to Those of Related Phases at (*P*, *T*) Conditions Close to 4.5 GPa, 600°C and at Ambient Conditions[a]

| Phase | (P, T) (GPa,°C) | Basal *d*-Spacing (Å) | $\nu$OH ($cm^{-1}$) at Ambient Conditions | Reference |
|---|---|---|---|---|
| Intermediate phase | 4.3, 631 | 9.57 | 3589, 3622, **3676**, 3701 | This study |
| 10 Å phase | 6.0, 647 | 9.39 | | *Chollet et al.* [2009] |
| 10 Å phase | ambient | 10.04 | 3593, **3622**, 3669 | *Chollet et al.* [2009] |
| 10 Å phase | ambient | 9.93–10.07 | 3593, **3622**, 3668 | *Fumagalli et al.* [2001] |
| Acetone treated 10 Å phase | ambient | 9.64–10.07 | 3593, 3620, **3675** | *Fumagalli et al.* [2001] |
| Talc | 4.6, 641 | 8.92 | | *Chollet et al.* [2009] |
| Talc | ambient | 9.37 | **3679** | *Chollet et al.* [2009] |
| Recrystallization phase | 6.0, 647 | 9.58 | **3674** | *Chollet et al.* [2009] |
| Talc-like phase | ambient | 10.28 | 3600, 3675, **3710** | *Perrillat et al.* [2005] |

[a]Bold values represent the most intense OH stretching vibration frequency for each phase.

gorite still represents ~65% of the intermediate assemblage after 80 min reaction, suggesting that only ~35% of the initial antigorite transformed into olivine + intermediate hydrous phase during step 1. A close look at the summed intensity of olivine X-ray diffraction lines reveals that the amount of olivine produced during step 1 corresponds to 44 ± 2% of the final amount of olivine (Figure 2). Assuming the complete dehydration of antigorite is described by reaction (2) of *Wunder and Schreyer* [1997]:

$$1\ \text{antigorite} = 14\ \text{olivine} + 20\ \text{clinoenstatite} + 31\ \text{water}$$

Step 1 produces 6 olivine (44 ± 2% of 14 olivine) and a small amount of 10 Å phase from the breakdown of ~1/3 of the initial amount of antigorite (35%). Those proportions correspond to reaction (23) of *Wunder and Schreyer* [1997]:

$$1\ \text{antigorite} = 18\ \text{olivine} + 4\ 10\ \text{Å}\ \text{phase} + 19\ \text{water}$$

The intermediate assemblage is therefore best described by 66 wt % of remaining antigorite, and 19 wt % olivine, 12 wt % 10 Å phase, and 3 wt % water. Reaction (23) of *Wunder and Schreyer* [1997] was already reported as a possible antigorite breakdown reaction by *Khodyrev and Agoshkov* [1986] and *Ulmer and Trommsdorff* [1995] but was discarded under equilibrium conditions in the $MgO$-$SiO_2$-$H_2O$ (MSH) system at pressure below 6 GPa [*Bromiley and Pawley*, 2002; *Wunder and Schreyer*, 1997]. The present investigation of the intermediate stage indicates that the initiation of antigorite breakdown involves partial transformation into olivine and 10 Å phase prior to complete dehydration. Only 25 wt % of the initial amount of water stored as hydroxyl groups in antigorite is liberated as free water during step 1. The remaining 75 wt % of mineral-bound water are still stored in antigorite (66 wt %) and in the intermediate hydrous phase (9 wt %).

### 3.3. Kinetics of Dehydration and Fluid Production Rate

[16] Fluid production rates during antigorite dehydration were calculated from kinetic data, following *Chollet et al.* [2009]. Most of the water (75 wt %) is released during step 2, which is therefore the major dehydration step. The summed intensity of selected diffraction lines as a function of time, designed by $I(t)$, for each hydrous mineral was fitted according to the Avrami equation [*Avrami*, 1939]:

$$I(t) = I_{\max}[1 - \exp(-k\,t^n)] \quad (1)$$

where $I_{\max}$ is the intensity before the transformation started, measured in the last spectrum prior to the onset of the transformation, $k$ is the constant rate in $s^{-n}$, and $n$ is the Avrami parameter which depends on the mechanism of the transformation. Values of $k$ are refined by a least squares method for a range of $n$ values (from 0.5 to 4 at increment of 0.5). Results for both hydrous phases are given in Table 2. Values of $n$ for the decay of antigorite and 10 Å phase equal 2 and 4, respectively, for the highest correlation coefficient. This latter value prevents us from using the growth rate laws developed for $n$ values of 1, 2, or 3 by *Cahn* [1956]. Alternatively, dehydration rates can also be obtained from the half-lifetimes of the reaction $t_{1/2}$ when half of both hydrous phases has disappeared after the onset of step 2. Half of the antigorite and half of the 10 Å phase disappeared 15 min and 19 min, respectively, after step 2 started. The antigorite and 10 Å phase dehydration half-lifetimes obtained in the present study compare well with those measured for talc and 10 Å phase ranging between 3 min and 78 min in the same (*P*, *T*) range [*Chollet et al.*, 2009]. We determine the fluid production rate $V_{1/2,\,fluid}$ ($m^3_{\text{fluid}}\ m^3_{\text{rock}}\ s^{-1}$) from the inverse half-lifetimes of antigorite and 10 Å phase, respectively:

$$V_{1/2,\,fluid} = \frac{H_2O}{t_{1/2}}\,\frac{\rho}{\rho_{H_2O}} \quad (2)$$

with $H_2O$ the water content of the mineral, $\rho$ its density, and $\rho_{H_2O}$ the density of water at the same (*P*, *T*) conditions. Antigorite and 10 Å phase are assumed to contain 13 and 9.1 wt % $H_2O$, respectively. Mineral densities result from refinement of the present X-ray diffraction data. The density of water $\rho_{H_2O}$ is from *Zhang and Duan* [2005]. This leads to a fluid production rate during antigorite dehydration of $10^{-4}\ m^3_{\text{fluid}}\ m^{-3}_{\text{rock}}\ s^{-1}$ (Table 1).

[17] This fluid production rate during antigorite dehydration in a closed system is very fast. For comparison, fluid production rate during antigorite dehydration in an open system was calculated from half-lifetimes after *Perrillat et al.* [2005]. Considering only the reaction forsterite + "talc-like" phase = enstatite + $H_2O$ and for (*P*, *T*) conditions close to those in this study, those rates are slightly lower, ~$5 \times 10^{-5}\ m^3_{\text{fluid}}\ m^3_{\text{rock}}\ s^{-1}$, than ours. Although counterintuitive, the fluid production rate under lower water activity is slower than at higher water activity. This is due to the fact that in the open system the intermediate assemblage retains only ~40% of the initial water content stored in the talc-like phase prior to final dehydration, while in the closed system

**Table 2.** Kinetics Parameters $k$ and $n$ and Details of Fluid Production Rate Calculations for Both Hydrous Phases During Step 2 of Antigorite Dehydration at 681°C, 4.1 GPa[a]

| Phase | $n$ | $k$ | $t_{1/2}$ (s) | Percent $H_2O$ | $\rho_{H_2O}$ | $\rho$ | $V_{1/2}$ ($s^{-1}$) | Weight Percent | $V_{fluid}$ ($m^3_{fluid}$ $m^{-3}_{rock}$ $s^{-1}$) |
|---|---|---|---|---|---|---|---|---|---|
| Antigorite | 2 | $9.05 \times 10^{-7}$ | 875 | 13 | 1327 | 2.55 | $1.43 \times 10^{-4}$ | 66 | $9.42 \times 10^{-5}$ |
| Intermediate phyllosilicate | 4 | $4.44 \times 10^{-13}$ | 1118 | 9.1 | 1327 | 2.70 | $8.28 \times 10^{-5}$ | 12 | $9.09 \times 10^{-6}$ |
| Sum | | | | | | | | | $1.05 \times 10^{-4}$ |

[a]Values of $k$ and $n$ were calculated from a least squares method fit of the data to Avrami equation; $t_{1/2}$ is the time for which half of hydrous phase disappeared, $\rho_{H_2O}$ is from *Zhang and Duan* [2005], mineral densities $\rho$ are from the present XRD data, $V_{1/2}$ is the speed of fluid release for each hydrous mineral, $V_{fluid}$ is the fluid production rate per unit volume of rocks per unit volume of time, and the proportion of each hydrous phase in the sample after step 1 is estimated from BSE images.

we estimate that 75% of the initial water content is still present in the intermediate assemblage in both antigorite and the intermediate hydrous phase. Ultimately, this shows that fluid production rates during antigorite dehydration reaction are very high and only slightly affected by water activity.

[18] At equilibrium, the rate of fluid production equals zero by definition. The rules of non equilibrium thermodynamics [*de Groot and Mazur*, 1984] indicate that the kinetics of a reaction increases with the distance from equilibrium and can be written in the form

$$V_{fluid} = F(P - Pe - \gamma(T - Te)) \tag{3}$$

where $\gamma$ is the Clapeyron slope of the reaction and $F$ is an increasing function vanishing at equilibrium. $Pe$ and $Te$ are the equilibrium pressure and temperature. Unfortunately, we are not able to determine the function $F$ from the present experimental data set. Our ($P$, $T$) condition measurements do show that experimental pressures were controlled to within $\Delta P$ = 0.4 GPa. The reaction rate is most likely increasing with pressure within a narrow pressure range smaller than $\Delta P$. The rate is then observed to saturate around $V_{1/2,\,fluid}$. Consequently, for further geodynamic applications the reaction rate should be considered faster than

$$V_{fluid} = \frac{V_{1/2,\,fluid}}{\Delta P}(P - Pe - \gamma(T - Te)). \tag{4}$$

Such a high fluid production rate is compared in section 3.4 with the deformation properties of minerals and rocks in the subducting slab or nearby in the mantle wedge.

### 3.4. Consequences for Subduction Zone Seismicity

[19] Competition between the fluid production rate and the rate of solid matrix deformation governed by the weakest phase, determines the mechanical imbalance formed during the reaction and ultimately triggers a rupture. The mechanical effects of dehydration reactions, including the effects of antigorite dehydration, in subduction zones were studied in detail by *Miller et al.* [2003]. Dehydration reactions usually result in an overpressure if the volume of the reaction products is greater than the porosity created by the reaction. Fluid pressure may rise, leading to the reduction of effective overburden pressure and ultimately to brittle deformation [*Raleigh and Paterson*, 1965]. Then, the fluid pressure is reduced from the increase in crack porosity and/or from hydraulic communication with a low-pressure region. This general case should in principle not apply to antigorite dehydration at pressure in excess of 2 GPa, where the Clapeyron slope of the dehydration reaction turns negative (Figure 3). However, a number of experiments conducted on serpentinite above 2 GPa, have produced brittle hydrofractures during antigorite dehydration [*Dobson et al.*, 2002; *Jung and Green*, 2004; *Jung et al.*, 2004, 2009]. Field evidence of brittle hydrofractures linked to antigorite dehydration at 2–2.5 GPa were recently recognized in previously subducted serpentinite samples of the Erro-Tobbio region in the Alps [*Healy et al.*, 2009]. Both experimental and field evidence of dehydration embrittlement above 2 GPa show that the pore fluid pressure must have increased during antigorite dehydration and reduced the effective normal stress sufficiently to bring the system into the brittle regime. Such an interpretation suggests that the coupling between dehydration and porosity generation actually allowed pressurization of the evolved aqueous fluid, despite the negative Clapeyron slope of the dehydration reaction. We speculate that the effective volume change at the equilibrium reaction boundary is not applicable in describing volume changes of a dynamically reacting system such as the one studied here. With a reduced effective overburden pressure, the system is expected to behave as described in lower total pressure experiments on serpentine dehydration [e.g., *Raleigh and Paterson*, 1965; *Tenthorey and Cox*, 2003; *Llana-Fúnez et al.*, 2007; *Rutter et al.*, 2009]. Generation of pore pressure excess occurs as the first consequence of dehydration, followed by the development of an interconnected pore network and a permeable network [*Ko et al.*, 1997; *Wong et al.*, 1997]. The fluid production rate obtained in this study during dehydration of antigorite at 4.5 ± 0.2 GPa is high enough to support the development of high pore fluid pressures either locally in serpentinites at the dehydration front, or further away in stronger units that may have been previously faulted, due to the high permeability that typically develops in presence of a large fluid flux.

[20] The nucleation of hydrofractures at the dehydration front observed in high-pressure experiments, or at a larger scale in the alpine serpentinites results from a combination of the very high fluid production rate and the high effective confining pressure that drives any porosity to collapse in a serpentinite matrix that has a typical relaxation rate of $3 \times 10^{-7}$ to $3 \times 10^{-12}$ $s^{-1}$ at ($P$, $T$) conditions of subduction zone [*Hilairet et al.*, 2007]. Although the weakest mineral in surrounding rocks, antigorite has a relaxation rate that is much slower than the fluid production rate of $10^{-4}$ $m^3_{fluid}$ $m^{-3}_{rock}$ $s^{-1}$. The high fluid production rate is also very favorable to fluid drainage through the induced permeable network in previously faulted zones in the slab [*Tenthorey and Cox*, 2003]. Fossil faults could be

reactivated and lead to rupture, a mechanism that is consistent with double-couple events observed for intermediate-depth earthquakes [*Dobson et al.*, 2002; *Hacker et al.*, 2003].

[21] The amount of water released by antigorite dehydration in dipping slabs may be large, since extensive serpentinization of the oceanic plate (up to 60%) is observed by seismic velocity anomalies [e.g., *Kawakatsu and Watada*, 2007; *Zhao et al.*, 1992] as well as by sampling ultramafic rocks of transform faults on the oceanic floor [e.g., *Cannat and Seyler*, 1995]. The lithosphere may be serpentinized down to a depth of 20–30 km by fluids infiltration through outer rise normal faulting [*Ranero et al.*, 2003] or through sub-Rayleigh convection that supply water in discrete and sparse fractures of the oceanic plate [*Wang*, 2002].

[22] Consequently, the very high fluid production rate caused by antigorite dehydration is suitable to trigger seismicity of the lower plane of the DSZ, either directly at the dehydration front or in the surrounding rocks. In a previous study, we showed that the fluid production rate during the dehydration of talc and 10 Å phase is also very fast, $10^{-4}$ to $10^{-5}$ $m^3_{fluid}$ $m^{-3}_{rock}$ $s^{-1}$ [*Chollet et al.*, 2009]. Accordingly, the few dehydration kinetics results available so far for hydrous minerals present in subducted rocks (namely antigorite, talc and 10 Å phase) support the classical hypothesis drawn from the comparison between stability fields of hydrous minerals and hypocenter locations that dehydration is a probable cause of intermediate depth earthquake. If high rates of fluid production in the order $10^{-4}$ to $10^{-5}$ $m^3_{fluid}$ $m^{-3}_{rock}$ $s^{-1}$ are characteristic to dehydration reactions, then chlorite dehydration might well explain earthquakes under warmer conditions [*Hacker et al.*, 2003; *Brudzinski et al.*, 2007]. More generally as suggested by *Omori et al.* [2004] earthquake hypocenters might locate devolatilization in the slab.

[23] **Acknowledgments.** We warmly thank J.-P. Perrillat for fruitful comments. The manuscript also benefited from an animated discussion with F. Brunet, S. Poli, and Y. Ricard during the Ph.D. defense of M. Chollet. Constructive reviews and comments by anonymous reviewers and the Associate Editor W. van Westrenen helped to improve the manuscript. The facility for Raman spectroscopy at the Ecole Normale Supérieure de Lyon is supported by the Institut National des Sciences de l'Univers. This study was supported by ANR project SUBDEF grant ANR-08-BLAN-0192.

## References

Auzende, A.-L., I. Daniel, B. Reynard, C. Lemaire, and F. Guyot (2004), High-pressure behaviour of serpentine minerals: A Raman spectroscopic study, *Phys. Chem. Miner.*, *31*, 269–277, doi:10.1007/s00269-004-0384-0.

Avrami, M. (1939), Kinetics of phase change, *J. Chem. Phys.*, *7*, 1103–1112, doi:10.1063/1.1750380.

Bauer, J. F., and C. B. Sclar (1981), The '10Å phase' in the system $MgO$-$SiO_2$-$H_2O$, *Am. Mineral.*, *66*, 576–585.

Besson, J.-M., G. Hamel, T. Grima, R. J. Nelmes, J. S. Loveday, S. Hull, and D. Hausermann (1992), A large volume pressure cell for high pressure, *High Pressure Res.*, *8*, 625–630, doi:10.1080/08957959208206312.

Bose, K., and A. Navrostsky (1998), Thermochemistry and phase equilibria of hydrous phases in the system $MgO$-$SiO_2$-$H_2O$: Implications for volatile transport to the mantle, *J. Geophys. Res.*, *103*, 9713–9719, doi:10.1029/98JB00506.

Bromiley, G. D., and A. R. Pawley (2002), The high-pressure stability of Mg-sursassite in a model hydrous peridotite: A possible mechanism for the deep subduction of significant volumes of $H_2O$, *Contrib. Mineral. Petrol.*, *142*, 714–723, doi:10.1007/s00410-001-0318-5.

Bromiley, G. D., and A. R. Pawley (2003), The stability field in the systems $MgO$-$SiO_2$-$H_2O$ (MSH) and $MgO$-$Al_2O_3$-$SiO_2$-$H_2O$ (MASH): The effects of $Al^{3+}$ substitution on high pressure stability, *Am. Mineral.*, *88*, 99–108.

Brudzinski, M. R., C. H. Thurber, B. R. Hacker, and E. R. Engdahl (2007), Global prevalence of double Benioff zones, *Science*, *316*, 1472–1474, doi:10.1126/science.1139204.

Cahn, J. W. (1956), The kinetics of grain boundary nucleated reactions, *Acta Metall.*, *4*, 449–459, doi:10.1016/0001-6160(56)90041-4.

Candela, P. A., C. D. Crummett, D. J. Earnest, M. R. Frank, and A. G. Wylie (2007), Low-pressure decomposition of chrysotile as a function of time and temperature, *Am. Mineral.*, *92*, 1704–1713, doi:10.2138/am.2007.2559.

Cannat, M., and M. Seyler (1995), Transform tectonics, metamorphic plagioclase and amphibolitization in ultramafic rocks of the Vema transform fault (Atlantic Ocean), *Earth Planet. Sci. Lett.*, *133*, 283–298, doi:10.1016/0012-821X(95)00078-Q.

Chinnery, N. J., A. R. Pawley, and S. M. Clark (1999), In situ observation of the formation of 10 Å phase from talc + $H_2O$ at mantle pressures and temperatures, *Science*, *286*, 940–942, doi:10.1126/science.286.5441.940.

Chollet, M., I. Daniel, K. T. Koga, S. Petitgirard, and G. Morard (2009), Dehydration kinetics of talc and 10 Å phase: Consequences for subduction zone seismicity, *Earth Planet. Sci. Lett.*, *284*, 57–64, doi:10.1016/j.epsl.2009.04.008.

Crichton, W., and M. Mezouar (2002), Noninvasive pressure and temperature estimation in large-volume apparatus by equation-of-state cross-calibration, *High Temp. High Pressures*, *34*, 235–242, doi:10.1068/htjr019.

de Groot, S. R., and P. Mazur (1984), *Non-Equilibrium Thermodynamics*, 544 pp., Dover, Amsterdam.

Dobson, D. P., P. G. Meredith, and S. A. Boon (2002), Simulation of subduction zone seismicity by dehydration of serpentine, *Science*, *298*, 1407–1410, doi:10.1126/science.1075390.

Dorbath, C., M. Gerbault, G. Carlier, and M. Guiraud (2008), Double seismic zone of the Nazca plate in northern Chile: High-resolution velocity structure, petrological implications, and thermomechanical modeling, *Geochem. Geophys. Geosyst.*, *9*, Q07006, doi:10.1029/2008GC002020.

Eggler, D. H., and A. N. Ehmann (2010), Rate of antigorite dehydration at 2 GPa applied to subduction zones, *Am. Mineral.*, *95*, 761–769, doi:10.2138/am.2010.3227.

Frank, M. R., P. A. Candela, D. J. Earnest, and A. G. Wylie (2005), Experimental study of the thermal decomposition of lizradite up to 973 K, *Geol. Soc. Am. Abstr. Programs*, *37*, 271.

Fumagalli, P., and L. Stixrude (2007), The 10 Å phase at high pressure by first principles calculations and implications for the petrology of subduction zones, *Earth Planet. Sci. Lett.*, *260*, 212–226, doi:10.1016/j.epsl.2007.05.030.

Fumagalli, P., L. Stixrude, S. Poli, and D. Snyder (2001), The 10 Å phase: A high-pressure expandable sheet silicate stable during subduction of hydrated lithosphere, *Earth Planet. Sci. Lett.*, *186*, 125–141, doi:10.1016/S0012-821X(01)00238-2.

Guillot, S., K. H. Hattori, J. de Sigoyer, T. Nägler, and A.-L. Auzende (2001), Evidences of hydration of the mantle wedge and its role in the exhumation of eclogites, *Earth Planet. Sci. Lett.*, *193*, 115–127, doi:10.1016/S0012-821X(01)00490-3.

Hacker, B. R., S. M. Peacock, G. A. Abers, and S. D. Holloway (2003), Subduction factory: 2. Are intermediate-depth earthquakes in subducting slabs linked to metamorphic dehydration reactions?, *J. Geophys. Res.*, *108*(B1), 2030, doi:10.1029/2001JB001129.

Hasegawa, A., N. Umino, and A. Takagi (1978), Double-planed deep seismic zone and upper mantle structure in the northeastern Japan arc, *Geophys. J. R. Astron. Soc.*, *54*, 281–296, doi:10.1111/j.1365-246X.1978.tb04260.x.

Healy, D., S. M. Reddy, N. E. Timms, E. M. Gray, and A. Vitale Brovarone (2009), Trench-parallel fast axes of seismic anisotropy due to fluid-filled carck in subducting slabs, *Earth Planet. Sci. Lett.*, *283*, 75–86, doi:10.1016/j.epsl.2009.03.037.

Hermann, J., O. Müntener, and M. Scambelluri (2000), The importance of serpentinite mylonites for subduction and exhumation of oceanic crust, *Tectonophysics*, *327*, 225–238, doi:10.1016/S0040-1951(00)00171-2.

Hilairet, N., I. Daniel, and B. Reynard (2006), Equation of state of antigorite, stability field of serpentines, and seismicity in subduction zones, *Geophys. Res. Lett.*, *33*, L02302, doi:10.1029/2005GL024728.

Hilairet, N., B. Reynard, Y. Wang, I. Daniel, S. Merkel, N. Nishiyama, and S. Petitgirard (2007), High-pressure creep of serpentine, interseismic deformation, and initiation of subduction, *Science*, *318*, 1910–1913, doi:10.1126/science.1148494.

Inoue, T., I. Yoshimi, A. Yamada, and T. Kikegawa (2009), Time-resolved diffraction analysis of the experimental dehydration of serpentine at high pressure, *J. Mineral. Petrol. Sci.*, *104*, 105–109, doi:10.2465/jmps.081022d.

Jung, H., and H. W. Green (2004), Experimental faulting of serpentinite during dehydration: Implications for earthquakes, seismic low-velocity

zones, and anomalous hypocenter distributions in subduction zones, *Int. Geol. Rev.*, *46*(12), 1089–1102, doi:10.2747/0020-6814.46.12.1089.

Jung, H., et al. (2004), Intermediate-depth earthquake faulting by dehydration embrittlement with negative volume change, *Nature*, *428*, 545–549, doi:10.1038/nature02412.

Jung, H., et al. (2009), Frictional sliding in serpentine at very high pressure, *Earth Planet. Sci. Lett.*, *277*, 273–279, doi:10.1016/j.epsl.2008.10.019.

Kawakatsu, H., and S. Watada (2007), Seismic evidence for deep-water transportation in the mantle, *Science*, *316*, 1468–1471, doi:10.1126/science.1140855.

Khodyrev, O., and V. Agoshkov (1986), Phase transformations of serpentine in the system $MgO$-$SiO_2$-$H_2O$ at the pressure range 40 to 80 kbar, *Geokhimiya*, *2*, 264–269.

Ko, S.-c., D. L. Olgaard, and T.-f. Wong (1997), Generation and maintenance of pore pressure excess in a dehydrating system: 1. Experimental and microstructural observations, *J. Geophys. Res.*, *102*, 825–839, doi:10.1029/96JB02485.

Koga, K. T., I. Daniel, and B. Reynard (2005), Determination of trace element partition coefficients between water and minerals by high-pressure and high temperature experiments: Leaching technique, *Geochem. Geophys. Geosyst.*, *6*, Q09014, doi:10.1029/2005GC000944.

Komabayashi, T., K. Hirose, K. Funakoshi, and N. Takafuji (2005), Stability of phase A in antigorite (serpentine) composition determined by in situ X-ray pressure observations, *Phys. Earth Planet. Inter.*, *151*, 276–289, doi:10.1016/j.pepi.2005.04.002.

Larson, A. C., and R. B. Von Dreele (2004), General Structure Analysis System (GSAS), *Los Alamos Natl. Lab. Rep., LAUR 86-748*.

Le Bail, A., H. Duroy, and J. L. Fourquet (1988), Ab-initio structure determination of $LiSbWO_6$ by X-ray powder diffraction, *Mater. Res. Bull.*, *23*, 447–452, doi:10.1016/0025-5408(88)90019-0.

Llana-Fúnez, S., H. K. Brodie, E. H. Rutter, and J. C. Arkwright (2007), Experimental dehydration kinetics of serpentine using pore volumetry, *J. Metamorph. Geol.*, *25*, 423–438, doi:10.1111/j.1525-1314.2007.00703.x.

Mezouar, M., T. Le Bihan, H. Libotte, Y. Le Godec, and D. Hausermann (1999), Paris-Edinburgh large-volume cell coupled with a fast imaging-plate system for structural investigation at high pressure and high temperature, *J. Synchrotron Radiat.*, *6*, 1115–1119, doi:10.1107/S0909049599010651.

Miller, S. A., W. v. d Zee, D. L. Olgaard, and J. A. D. Connoly, (2003), A fluid-pressure feedback model of dehydration reactions: experiments, modelling, and application to subduction zones, *Tectonophysics*, *370*, 241–251, doi:10.1016/S0040-1951(03)00189-6.

Morard, G. (2006), Les systèmes Fe-FeS et Fe-s-Si à haute pression et haute température. Implications pour les noyaux des corps planétaires, Ph.D. thesis, Inst. de Phys. du Globe de Paris, Paris.

Niskanen, E. (1964), Reduction of orientation effects in quantitative X-ray diffraction analysis of kaolin minerals, *Am. Mineral.*, *49*, 705–714.

Omori, S., S. Kamiya, S. Maruyama, and D. Zhao (2002), Morphology of the intraslab seismic zone and devolatilization phase equilibria of the subducting slab peridotite, *Bull. Earthquake Res. Inst. Univ. Tokyo*, *76*, 455–478.

Omori, S., et al. (2004), Dehydration and earthquakes in the subducting slab: empirical link in intermediate and deep seismic zones, *Phys. Earth Planet. Inter.*, *146*, 297–311, doi:10.1016/j.pepi.2003.08.014.

Peacock, S. M. (2001), Are the lower planes of double seismic zones caused by serpentine dehydration in subducting oceanic mantle?, *Geology*, *29*, 299–302, doi:10.1130/0091-7613(2001)029<0299:ATLPOD>2.0.CO;2.

Perrillat, J.-P., I. Daniel, K. T. Koga, B. Reynard, H. Cardon, and W. A. Crichton (2005), Kinetics of antigorite dehydration: A real-time X-ray diffraction study, *Earth Planet. Sci. Lett.*, *236*, 899–913, doi:10.1016/j.epsl.2005.06.006.

Raleigh, C. B., and M. S. Paterson (1965), Experimental deformation of serpentine and its tectonic implications, *J. Geophys. Res.*, *70*(16), 3965–3985, doi:10.1029/JZ070i016p03965.

Ranero, C. R., J. Phipps Morgan, K. McIntosh, and C. Reichert (2003), Bonding-related faulting and mantle serpentinization at the Middle America trench, *Nature*, *425*, 367–373, doi:10.1038/nature01961.

Rüpke, L. H., J. P. Morgan, M. Hort, and J. A. D. Connoly (2004), Serpentine and subduction zone water cycle, *Earth Planet. Sci. Lett.*, *223*, 17–34, doi:10.1016/j.epsl.2004.04.018.

Rutter, E. H., S. Llana-Funez, and K. H. Brodie (2009), Dehydration and deformation of intact cylinders of serpentinite, *J. Struct. Geol.*, *31*, 29–43, doi:10.1016/j.jsg.2008.09.008.

Takemura, K. (2001), Evaluation of the hydrostaticity of a helium-pressure medium with powder X-ray diffraction techniques, *J. Appl. Phys.*, *89*, 662–668, doi:10.1063/1.1328410.

Tenthorey, E., and S. F. Cox (2003), Reaction-enhanced permeability during serpentinite dehydration, *Geology*, *31*, 921–924, doi:10.1130/G19724.1.

Ulmer, P., and V. Trommsdorff (1995), Serpentine stability to mantle depths and subduction-related magmatism, *Science*, *268*, 858–861, doi:10.1126/science.268.5212.858.

Wang, J., A. G. Kalinichev, and R. J. Kirkpatrick (2004), Molecular modeling of the 10-Å phase at subduction zone conditions, *Earth Planet. Sci. Lett.*, *222*, 517–527, doi:10.1016/j.epsl.2004.03.013.

Wang, K. (2002), Unbending combined with dehydration embrittlement as a cause for double and triple seismic zones, *Geophys. Res. Lett.*, *29*(18), 1889, doi:10.1029/2002GL015441.

Wong, T.-f., S.-c. Ko, and D. L. Olgaard (1997), Generation and maintenance of pore pressure excess in a dehydrating system: 2. Theoretical analysis, *J. Geophys. Res.*, *102*, 841–852, doi:10.1029/96JB02484.

Wunder, B., and W. Schreyer (1997), Antigorite: High-pressure stability in the system $MgO$-$SiO_2$-$H_2O$ (MSH), *Lithos*, *41*, 213–227, doi:10.1016/S0024-4937(97)82013-0.

Yamasaksi, T., and T. Seno (2003), Double seismic zone and dehydration embrittlement of the subducting slab, *J. Geophys. Res.*, *108*(B4), 2212, doi:10.1029/2002JB001918.

Yamamoto, S., I. Ohno, and O. L. Anderson (1987), High temperature elasticity of sodium chloride, *J. Phys. Chem. Solids*, *48*, 143–151, doi:10.1016/0022-3697(87)90078-3.

Zhang, Z., and Z. Duan (2005), Prediction of the PVT properties of water over wide range of temperatures and pressures from molecular dynamics simulation, *Phys. Earth Planet. Inter.*, *149*, 335–354, doi:10.1016/j.pepi.2004.11.003.

Zhao, D., A. Hasegawa, and S. Horiuchi (1992), Tomographic imaging of *P* and *S* wave velocity structure beneath northeastern Japan, *J. Geophys. Res.*, *97*, 19,909–19,928, doi:10.1029/92JB00603.

M. Chollet, I. Daniel, and B. van de Moortèle, Laboratoire de Géologie de Lyon: Terre, Planètes, Environnement, Université Lyon 1, Ecole Normale Supérieure de Lyon, CNRS, UMR 5276, 2 rue Raphael Dubois, F-69622 Villeurbanne CEDEX, France. (Isabelle.Daniel@univ-lyon1.fr)

K. T. Koga, Laboratoire Magmas et Volcans, UMR CNRS 6524, IRD M163, Université Blaise Pascal Clermont-Ferrand, 5 rue Kessler, F-63038 Clermont-Ferrand CEDEX, France.

G. Morard, European Synchrotron Radiation Facility, BP220, F-38043 Grenoble, France.